crystals

MDPI

Article

Stability, Elastic and Electronic Properties of Ta_2N by First-Principles Calculations

Longpeng Zhu [1], Jiong Wang [1,*], Chenchen Dong [1], Yong Du [1], Shun-Li Shang [2] and Zi-Kui Liu [2]

[1] Powder Metallurgy Research Institute, Central South University, Changsha 410083, China; 183311031@csu.edu.cn (L.Z.); Dongchenchen@csu.edu.cn (C.D.); yong-du@csu.edu.cn (Y.D.)
[2] Department of Materials Science and Engineering, The Pennsylvania State University, University Park, PA 16802, USA; sus26@psu.edu (S.-L.S.); Prof.zikui.liu@psu.edu (Z.-K.L.)
* Correspondence: wangjionga@csu.edu.cn

Abstract: Owing to exploring the influence of the N atoms ordering in Ta_2N compounds on their properties, the stability, elastic, and electronic properties of Ta_2N compounds (Ta_2N-I: $P\bar{3}m1$ and Ta_2N-II: $P\bar{3}1m$) were investigated using first-principles calculations based on density functional theory. Ta_2N-II is energetically favorable according to the enthalpy of formation. Elastic constants were employed to reveal the stronger resistance to deformation, but weaker anisotropy, in Ta_2N-II. A ductile-brittle transition was found between Ta_2N-I (ductile) and Ta_2N-II (brittle). The partial density of states showed a stronger orbital hybridization of Ta-d and N-p in Ta_2N-II, resulting in stronger covalent bonding. The charge density difference illustrated the interaction of the Ta-N bond and electron distribution of Ta_2N.

Keywords: first-principles calculations; Ta_2N compounds; tantalum nitride; elastic properties; electronic structure

check for updates

Citation: Zhu, L.; Wang, J.; Dong, C.; Du, Y.; Shang, S.-L.; Liu, Z.-K. Stability, Elastic and Electronic Properties of Ta_2N by First-Principles Calculations. *Crystals* **2021**, *11*, 445. https://doi.org/10.3390/cryst11040445

Academic Editor: Ray-Hua Horng

Received: 26 March 2021
Accepted: 15 April 2021
Published: 19 April 2021

Publisher's Note: MDPI stays neutral with regard to jurisdictional claims in published maps and institutional affiliations.

Copyright: © 2021 by the authors. Licensee MDPI, Basel, Switzerland. This article is an open access article distributed under the terms and conditions of the Creative Commons Attribution (CC BY) license (https://creativecommons.org/licenses/by/4.0/).

1. Introduction

The transition metal nitrides (TMNs) have widespread applications and motivate intense research because of their outstanding properties, such as good mechanical, thermal stability, electronic, and optical properties [1–6]. Tantalum nitrides (TaN_x) possess a series of equilibrium and metastable structures with various excellent properties, showing a remarkable richness of applications, including hard coatings for cutting tools, thin-film resistors, and diffusion barriers in integrated circuits [7–12]. The change of growth conditions generates different phase and chemical compositions of polycrystalline TaN_x, whose structures and properties vary greatly. Experimentally [7,13–17], ε-TaN (No.191, $P6/mmm$), π-TaN (No.189, $P\bar{6}2m$), δ-TaN (No.225, $Fm\bar{3}m$), ϑ-TaN (No.187, $P\bar{6}m2$), Ta_2N (No.162, $P\bar{3}1m$), Ta_3N_5 (No.63, $Cmcm$), Ta_4N_5 (No.87, $I4/m$), Ta_5N_6 (No. 193, $P6_3/mcm$), and η-Ta_2N_3 (No.62, $Pbnm$) etc., have been synthesized by controlling growth conditions, and have attracted further study on their properties. Limited by the imperfection of X-ray diffraction (XRD), the structural difference (slight shift of N) between ε-TaN and π-TaN had not been distinguished until the application of neutron diffraction [18]. After detailed investigation, a similar phenomenon was found in Ta_2N. In reality, there are two structures in Ta_2N compounds (which are called Ta_2N-I and Ta_2N-II for convenience in this work). Terao et al. [14] detected hexagonal close-packed γ-Ta_2N (Ta_2N-I), also called β-Ta_2N, with lattice parameters a = 3.05 Å, c = 4.92 Å (Space group, No.164) through XRD. Moreover, they also discovered the other structure of Ta_2N (Ta_2N-II) with lattice parameters a = 5.28 Å, c = 4.92 Å (Space group, No.162), due to a different ordering of N atoms, characterized by electron diffraction, which can display many weak peaks invisible in XRD. As the characterization techniques developed, neutron diffraction was employed by Conroy and Christensen to further confirm this structure (Ta_2N-II) [19]. It is because of the ordering of vacancies that Ta_2N-II come into being, which was presented by Friedrich et al. [20].

The same structure of Ta_2N-II was also found in Cr_2N [21], V_2N [22], and Nb_2N [23] compounds. By comparing the two structures of Ta_2N, it is found that partial N atoms migrate to the gap between two Ta atom layers and leave corresponding vacancies in the N atom layer. Thus, the atomic stacking model changes from N-Ta-Ta-N-Ta-Ta-⋯ of Ta_2N-I to N-Ta-N-Ta-⋯ of Ta_2N-II. To sum up, the shift of N atoms generates the vacancies of the initial N atom layers in Ta_2N-I, making a contribution to the formation of Ta_2N-II.

Compared to Ta_2N-II, Ta_2N-I was very exciting for researchers. Cu diffusion studies [24] applied using density functional theory (DFT) showed that Ta_2N-I can effectively prevent undesired Cu diffusion as an effective diffusion barrier material. The electronic and elastic properties of Ta_2N-I were explored using first-principles calculation by Yu et al. [25]. Hence, it is significant to explore the properties of Ta_2N-II, and clarify differences between Ta_2N-I and Ta_2N-II. In this work, the stability, elastic, and electronic properties of Ta_2N-I and Ta_2N-II were illustrated thoroughly using first-principles calculations based on DFT. The enthalpies of formation were calculated for stability comparison. Elastic constants were computed using a high-efficiency stress-strain method for elastic studies. Partial density of states (PDOS) and charge density difference (CDD) were applied for electronic research. Relevant results can promote the scientific study and commercial application of Ta_2N.

2. Model and Calculation Method

2.1. First-Principles Calculations

The crystal structure information of Ta_2N-I and Ta_2N-II with space groups $P\bar{3}m1$ and $P\bar{3}1m$, respectively, are shown in Table 1.

Table 1. Crystal structure information of Ta_2N-I and Ta_2N-II with space groups $P\bar{3}m1$ and $P\bar{3}1m$, respectively.

Structure	Space Group	Atom	Wyckoff Notation	x	y	z
Ta_2N-I	$P\bar{3}m1$	Ta	2d	1/3	2/3	z
		Ta	2d	2/3	1/3	z
		N	1a	0	0	0
Ta_2N-II	$P\bar{3}1m$	Ta	6k	1/3	0	z
		Ta	6k	2/3	0	z
		Ta	6k	0	1/3	z
		Ta	6k	0	2/3	z
		Ta	6k	1/3	1/3	z
		Ta	6k	2/3	2/3	z
		N	2d	1/3	2/3	1/2
		N	2d	2/3	1/3	1/2
		N	1a	0	0	0

Figure 1 illustrates clearly the difference of crystal structure from different viewpoints. First-principles calculations were used for the Ta_2N-I and Ta_2N-II using the Vienna Ab initio Simulation Package (VASP) 5.4.1 version [26,27]. The generalized gradient approximation (GGA) parameterized by Perdew-Burke-Ernzerhof (PBE) [28] and the projector augmented wave (PAW) [29] method, with an energy cut-off of 600 eV, were employed for the exchange-correlation effects and ion-electron interactions, respectively.

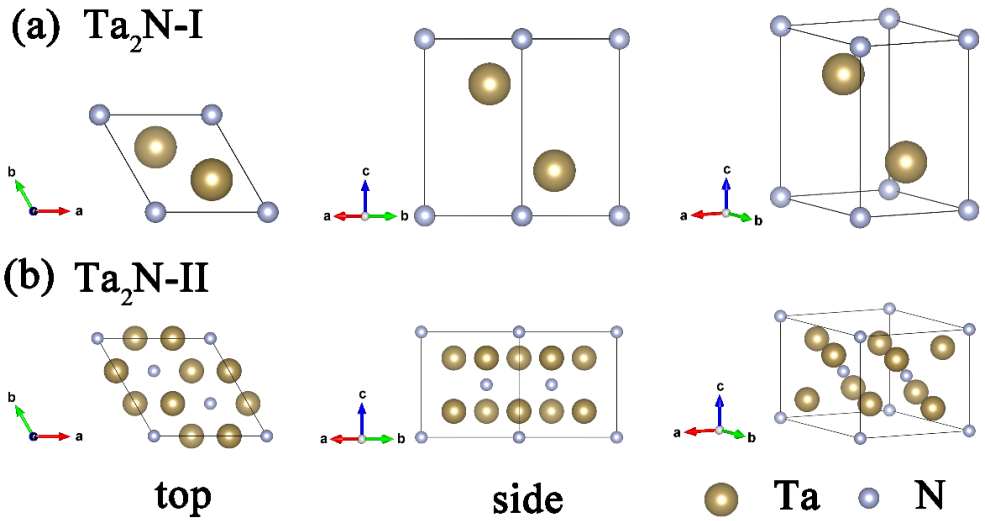

Figure 1. Structure sketch maps of (**a**) Ta_2N-I and (**b**) Ta_2N-II from different viewpoints.

The *k*-point meshes were Γ-centered 17 × 17 × 9, 9 × 9 × 11, 15 × 15 × 15 for the bulk Ta_2N-I, Ta_2N-II, bcc Ta; and 1 × 1 × 1 for the molecule (N_2), respectively. Herein, total energy calculations were performed in a large supercell of 14 Å × 15 Å × 16 Å for the N_2 molecule. The tetrahedron method with Blöchl corrections [30] was adopted for accurate total energy and electronic structure in integration of reciprocal space. The selected valence electrons were $5p^6 5d^6 6s^2$ for Ta, and $2s^2 2p^3$ for N. All systems were calculated with the convergence criteria 0.02 eV/Å for forces on ions, and 0.01 meV/atom for electrons, respectively.

In order to obtain the equilibrium structure, the four-parameter Birch-Murnaghan equation of state (EOS) was applied to fit the energy vs. volume (*E*-*V*) data points [31,32]:

$$E(V) = a + bV^{-\frac{2}{3}} + cV^{-\frac{3}{4}} + dV^{-\frac{3}{6}} \quad (1)$$

where *a*, *b*, *c*, and *d* are fitting parameters. This EOS can estimate the equilibrium total energy E_0, volume V_0, bulk modulus B_0, and its pressure derivative $B_0{}'$.

To compare Ta_2N-I and Ta_2N-II in terms of their thermodynamic stability, enthalpy of formation at 0 K, E_f (kJ/mol), was calculated as:

$$E_f = \frac{(E_{Ta_2N} - nE_{Ta} - \frac{n}{2}E_N)F}{N} \quad (2)$$

where E_{Ta_2N} is the total energy of Ta_2N, and E_{Ta}, E_N are the energy per atom of bcc Ta and one N_2 molecule, respectively. *n* and *N* are the atom numbers of Ta and all atoms in bulk Ta_2N. *F* is Faraday's constant.

The charge density difference (also called deformation charge density) can be calculated as [33]:

$$\Delta\rho = \rho(Ta_2N_{\text{self-consistent}}) - \rho(Ta_2N_{\text{atomic}}) \quad (3)$$

where $\rho(Ta_2N_{\text{self-consistent}})$ is the total charge densities obtained by self-consistent calculation. The superposition of the atomic charge densities, $\rho(Ta_2N_{\text{atomic}})$, can be acquired by non-self-consistent calculation.

2.2. Elastic Calculations

The elastic constants were calculated by the strain-stress method, as demonstrated by Shang et al. [6,34–36]. For this methodology, the strains ($\varepsilon = (\varepsilon_1, \varepsilon_2, \varepsilon_3, \varepsilon_4, \varepsilon_5, \varepsilon_6)$, where ε_1, ε_2, ε_3 are normal strains and ε_4, ε_5, ε_6 are shear strains) of a crystal are imposed through

specifying the lattice vectors in Cartesian coordinates, as shown in Equation (4). The lattice vectors, R, after deformation can be described as:

$$R = \begin{bmatrix} a_1 & a_2 & a_3 \\ b_1 & b_2 & b_3 \\ c_1 & c_2 & c_3 \end{bmatrix} \begin{bmatrix} 1+\varepsilon_1 & \varepsilon_6/2 & \varepsilon_5/2 \\ \varepsilon_6/2 & 1+\varepsilon_2 & \varepsilon_4/2 \\ \varepsilon_5/2 & \varepsilon_4/2 & 1+\varepsilon_3 \end{bmatrix} \tag{4}$$

where $\vec{a} = (a_1, a_2, a_3)$ is the lattice vector before deformation. $\vec{a}$, $\vec{b}$, and $\vec{c}$ are the same.

In this work, linearly independent and isotropic strains were used, and the strain was set to ± 0.01. By first-principles calculations, the corresponding set of stresses $\sigma = (\sigma_1, \sigma_2, \sigma_3, \sigma_4, \sigma_5, \sigma_6)$ of the deformed crystal with set of strains $\varepsilon = (\varepsilon_1, \varepsilon_2, \varepsilon_3, \varepsilon_4, \varepsilon_5, \varepsilon_6)$ could be obtained. The elastic constants (C_{ij}) are then acquired through the general Hook's law $C_{ij} = \varepsilon^{-1}\sigma$:

$$\begin{bmatrix} C_{11} & C_{12} & C_{13} & C_{14} & C_{15} & C_{16} \\ C_{21} & C_{22} & C_{23} & C_{24} & C_{25} & C_{26} \\ C_{31} & C_{32} & C_{33} & C_{34} & C_{35} & C_{36} \\ C_{41} & C_{42} & C_{43} & C_{44} & C_{45} & C_{46} \\ C_{51} & C_{52} & C_{53} & C_{54} & C_{55} & C_{56} \\ C_{61} & C_{62} & C_{63} & C_{64} & C_{65} & C_{66} \end{bmatrix} = \varepsilon^{-1}\sigma \tag{5}$$

This equation can be solved via the singular value decomposition method to get the least square solutions of the elastic constants.

For a trigonal crystal with space groups $P\bar{3}m1$ and $P\bar{3}1m$, there are six independent single crystal elastic constants (C_{11}, C_{12}, C_{13}, C_{14}, C_{33}, and C_{44}). The mechanical stability can be determined by the Born-Huang [37] criterion as:

$$C_{11} - |C_{12}| > 0, (C_{11} + C_{12})C_{33} > 2C_{13}^2, (C_{11} - C_{12})C_{44} > 2C_{14}^2 \tag{6}$$

Then, the Voigt and Reuss bounds of bulk modulus and shear modulus are [38]:

$$B_{\mathrm{V}} = \frac{1}{9}(2C_{11} + 2C_{12} + 4C_{13} + C_{33}) \tag{7}$$

$$B_{\mathrm{R}} = \frac{(C_{11} + C_{12})C_{33} - 2C_{13}^2}{(C_{11} + C_{12} - 4C_{13} + 2C_{33})} \tag{8}$$

$$G_{\mathrm{V}} = \frac{1}{30}(7C_{11} - 5C_{12} - 4C_{13} + 3C_{33} + 12C_{44}) \tag{9}$$

$$G_{\mathrm{R}} = \frac{15}{2}\left[\frac{2C_{11} + 2C_{12} + 4C_{13} + C_{33}}{(C_{11} + C_{12})C_{33} - 2C_{13}^2} + \frac{3C_{11} - 3C_{12} + 6C_{44}}{(C_{11} - C_{12})C_{44} - 2C_{14}^2}\right]^{-1} \tag{10}$$

Through the Viogt-Reuss-Hill approximation [39], the bulk modulus B, shear modulus G, Young's modulus E, and Poisson's ratio ν can be further obtained by:

$$B = \frac{1}{2}(B_{\mathrm{V}} + B_{\mathrm{R}}) \tag{11}$$

$$G = \frac{1}{2}(G_{\mathrm{V}} + G_{\mathrm{R}}) \tag{12}$$

$$E = \frac{9BG}{3B + G} \tag{13}$$

$$v = \frac{3B - 2G}{2(3B + G)} \tag{14}$$

The anisotropy of elastic properties can induce microcracks and reduce the mechanical durability. Thus, to characterize the elastic anisotropies, the universal elastic anisotropic index (A^{U}) [40] is described as follow:

$$A^{\mathrm{U}} = \frac{5G_{\mathrm{V}}}{G_{\mathrm{R}}} + \frac{B_{\mathrm{V}}}{B\mathrm{R}} - 6 \tag{15}$$

Besides, for trigonal crystals, the three-dimensional (3D) anisotropy of Young's modulus E can be obtained by the reciprocals of E [41]:

$$E^{-1} = S_{11}(1 - l_3^2) + S_{33}l_3^4 + (2S_{13} + S_{44})l_3^2(1 - l_3^2) + 2S_{14}l_2l_3(3l_1^2 - l_2^2) \tag{16}$$

where S_{ij} are the elastic compliance constants and l_{i} (i = 1, 2, 3) are the direction cosines:

$$l_1 = \sin\theta\cos\phi \tag{17}$$

$$l_2 = \sin\theta\sin\phi \tag{18}$$

$$l_3 = \cos\theta \tag{19}$$

here, θ is the angle between a certain direction and crystal orientation [001]. ϕ is crystal orientation [100]. The greater the deviation of the 3D anisotropy diagram from a sphere (isotropy) is, the higher the degree of anisotropy is.

3. Results and Discussions

3.1. Structure Stabilities

The differences of structure between Ta_2N-I and Ta_2N-II are illustrated in Figure 1 and Table 1. It was revealed that the shift of N atoms between layers changes the symmetry and atomic stacking model of Ta_2N-I, promoting the formation of Ta_2N-II. To compare the structure and stability of Ta_2N-I and Ta_2N-II, the lattice parameters and enthalpies of formation were calculated, as shown in Table 2. With regard to lattice parameters, a good agreement is shown between our calculated values and the reference data [14,19,24,25,42,43]. Especially, the calculated lattice parameters (a = 3.110 Å, c = 4.896 Å) of Ta_2N-I were very close to the results (a = 3.11 Å, c = 4.88 Å) [24] calculated through the same pseudo-potential (GGA-PBE), which confirms the reliability of this work.

Table 2. The calculated lattice parameters (Å) and enthalpies of formation E_{f} (kJ/mol) of Ta_2N-I and Ta_2N-II.

Method	Structure	Space Group	$a = b$ (Å)	c (Å)	Enthalpy of Formation (kJ/mol)
this work	Ta_2N-I	$P\bar{3}m1$	3.110	4.896	−78.61
Exp. [14]			3.05	4.92	-
Exp. [42]			3.047	4.918	−84.81
Exp. [43]			3.054	4.996	-
USPP-GGA [25]			3.1756	4.9433	-
PBE-GGA [24]			3.11	4.88	-
this work	Ta_2N-II	$P\bar{3}1m$	5.325	4.962	−89.43
Exp. [14]			5.28	4.92	-
Exp. [19]			5.285	4.919	-
GGA [23]			5.38	4.98	−95.62

In Figure 2, the total energies of Ta_2N-I and Ta_2N-II are plotted as a function of volume through Birch-Murnaghan equation of state fitting. It is shown that Ta_2N-II has lower energies in the whole variation range of volume. As for the enthalpies of formation, the negative values, −78.61 kJ/mol for Ta_2N-I and −89.43 kJ/mol for Ta_2N-II, declare that both structures are stable, agreeing well with experimental [42] and theoretical [23] results.

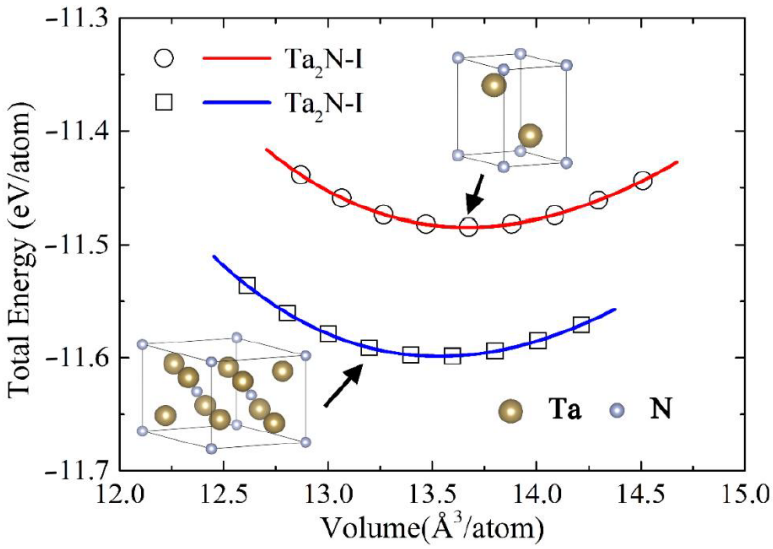

Figure 2. Equation of state fitting curve of energy-volume (*E*-*V*) for Ta_2N-I and Ta_2N-II.

It is worth noting that a more negative enthalpy of formation of Ta_2N-II means it is more energetically favorable than Ta_2N-I. Therefore, the ordering change of N atoms in Ta_2N-II brings a more stable atomic stacking model (N-Ta-N-Ta-⋯) for Ta_2N compound, comparing to the close-stacking (N-Ta-Ta-N-Ta-Ta-⋯) in Ta_2N-I. That is because the N atoms between the two Ta atom layers can generate covalent bond (Ta-N) layer by layer in Ta_2N-II but not in Ta_2N-I. In addition, Figure 3 demonstrates the variation of bond length between the two structures.

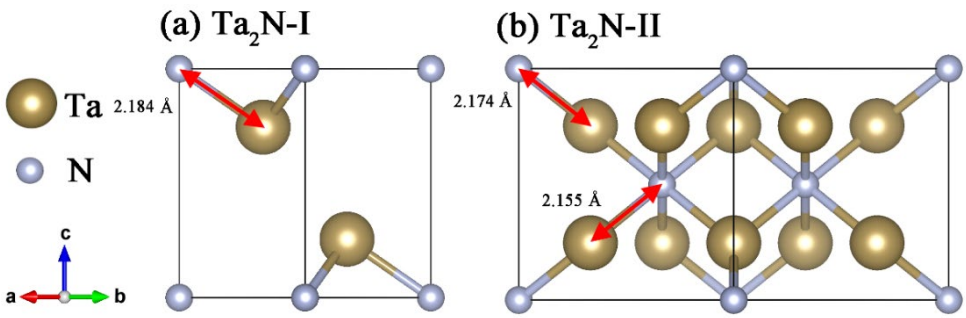

Figure 3. Comparison of the bond length (Å) variation of (**a**) Ta_2N-I and (**b**) Ta_2N-II.

Only one kind of Ta-N bond with the bond length 2.184 Å exists in Ta_2N-I. However, two types of Ta-N bond, with the shorter bond length (2.155 Å and 2.174 Å), are found in Ta_2N-II, owing to the different ordering of N atoms. The covalent bond (Ta-N) with a shorter bond length means a stronger bond strength. This also makes a contribution to the higher stability of Ta_2N-II.

3.2. Elastic Properties

To further investigate the difference in properties between Ta_2N-I and Ta_2N-II, elastic constants were calculated to reveal their elastic properties. There are six independent elastic constants in a trigonal system: C_{11}, C_{12}, C_{13}, C_{14}, C_{33}, and C_{44}, as shown in Table 3. According to the Born-Huang [37] criterion, both structures are mechanically stable. The difference between our calculated data of Ta_2N-I and the other theoretical values [25] was acceptable because of the different pseudo-potential (ultrasoft pseudo-potential, USPP) used for calculations. Comparing the C_{ij} of Ta_2N-I and Ta_2N-II, all the absolute values of C_{ij} increased except for C_{13} and C_{14}. The reduction of the C_{14} absolute value reveals that the Ta_2N-II became less anisotropic than Ta_2N-I.

Table 3. The calculated independent elastic constants C_{ij} (GPa) of Ta_2N-I and Ta_2N-II.

Method	Structure	C_{11}	C_{12}	C_{13}	C_{14}	C_{33}	C_{44}
this work	Ta_2N-I	440	136	214	−51	432	125
USPP-GGA [25]	-	403	125	215	−52	385	123
this work	Ta_2N-II	476	168	195	0	473	167

The calculated bulk modulus B, shear modulus G, Youngs' modulus E, Poisson's ratio ν, B/G ratio, the universal elastic anisotropic index A^{U}, and mechanical stability are summarized in Table 4. A crystal with a higher bulk modulus B signifies a lesser compressibility. Shear modulus G describes the resistance of a material to shear stress. Young's modulus is considered as a measure of the stiffness of a solid.

Table 4. The calculated bulk modulus B (GPa), shear modules G (GPa), Youngs' modulus E (GPa), Poisson's ratio ν, B/G ratio, universal elastic anisotropic index A^{U}, and mechanical stability of Ta_2N-I and Ta_2N-II.

Structure	B_{V}	B_{R}	B	G_{V}	G_{R}	G	E	v	B/G	A^{U}	Mechanical Stability
Ta_2N-I	271	269	270	145	113	129	334	0.29	2.09	1.42	stable
Ta_2N-II	282	282	282	171	154	163	410	0.26	1.73	0.55	stable

It was shown that Ta_2N-II possesses a higher bulk modulus B, shear modulus G, and Youngs' modulus E. This means Ta_2N-II is harder to deform than Ta_2N-I. In addition, the intrinsic ductility and brittleness of Ta_2N can be estimated by Poisson's ratio ν [44] and B/G ratio [45]. ν> (<)0.26, B/G ratio> (<)1.75 can be regarded as a performance index to distinguish brittle (ductile) materials. Notably, as shown in Table 4, the ν (0.29) and B/G ratio (2.09) decreased to 0.26 and 1.73 in the structural change from Ta_2N-I to Ta_2N-II, respectively. Namely, Ta_2N-I is ductile and Ta_2N-II is brittle. Hence, a different ordering of N atoms in Ta_2N-II leads to a ductile-brittle transition in Ta_2N compounds, which can markedly impact the mechanical properties. Furthermore, the universal elastic anisotropic index (A^{U}) and the 3D Young's modulus anisotropy were calculated to characterize the elastic anisotropy of Ta_2N compounds. Ta_2N-II with A^{U} = 0.55 behaved with a weaker elastic anisotropy than Ta_2N-I (1.42). Isotropic materials show the shape of a sphere in the 3D diagram of Young's modulus anisotropy. Figure 4 clearly demonstrates the difference of anisotropy between Ta_2N-I and Ta_2N-II. Obviously, the shape is more like a sphere in Figure 4b, corresponding to the weaker anisotropy of Ta_2N-II. A crystal with weaker anisotropy means the possibility of stress concentration is lower and the microcracks are harder to extend. Therefore, the higher resistance to deformation of Ta_2N-II was further confirmed.

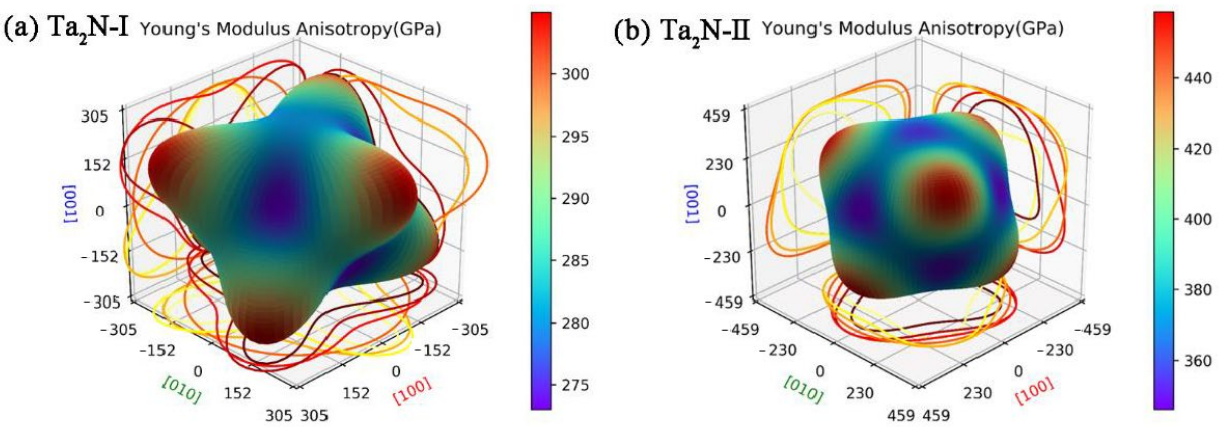

Figure 4. The three-dimensional anisotropy diagram of Young's modulus E of (**a**) Ta_2N-I and (**b**) Ta_2N-II.

3.3. Electronic Properties

To further probe the influence of the ordering change of N atoms in Ta_2N compounds, the total and partial density of states were calculated, and are presented in Figure 5. Comparing Figure 5a,b, the similarities of the two structures are as follows.

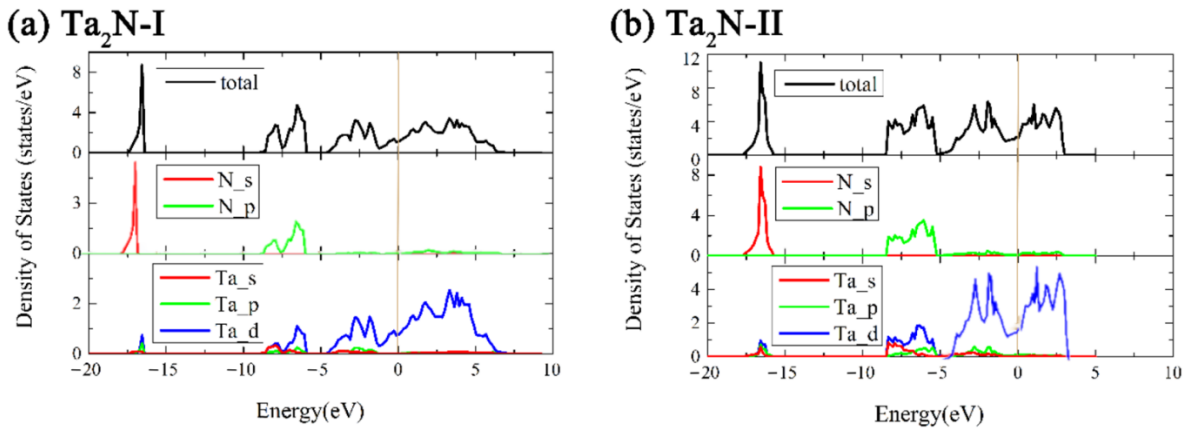

Figure 5. Total and partial density of states (**a**) Ta_2N-I and (**b**) Ta_2N-II. The vertical line denotes the Fermi energy level.

The positive values of DOS at the Fermi level indicate the metallic characteristic of Ta_2N-I and Ta_2N-II. The conduction bands and the upper valence bands (−5~0 eV) mainly consist of Ta-d states. While, the middle valence bands (−10~−5 eV) are primarily dominated by Ta-d states and N-p states. N-s states occupy the lower valence bands around −17 eV. Both Ta_2N-I and Ta_2N-II revealed the hybridization between N-p and Ta-d orbitals, proving the formation of the covalent bond, which was confirmed to be favorable to the hardness and shear resistance of the materials [46]. However, the energy region of Ta-N hybridization broadens (from −6~−8eV to −5~−8eV) in Ta_2N-II. It is implied that the ordering change of N atoms enhances the hybridization of Ta-d and N-p states and the overlaps of valence bonds between N and Ta atoms. The shorter bond lengths in Figure 3 of Ta-N bond in Ta_2N-II also contribute to the hybridization enhancement. This can explain the elevation of shear modulus in Ta_2N-II. Furthermore, the max energy of density of states distribution decreases from 7 eV in Ta_2N-I, to 3 eV in Ta_2N-II, which is beneficial to the higher stability of Ta_2N-II.

For analyzing the bonding interaction and electron transfer of Ta and N atoms, charge density difference was calculated, as shown in Figure 6. Herein, Figure 6a,b illustrate the sectional view of charge density difference of the (110) lattice plane in Ta_2N-I and the (100) lattice plane in Ta_2N-II, respectively. The lattice plane (110) of Ta_2N-I and (100) of Ta_2N-II are equivalent. The red areas denote the gain in electrons, and the blue areas are the loss of electrons.

Moreover, Figure 6c–f exhibit the side and top view of charge density difference of Ta_2N-I and Ta_2N-II, in which the blue and yellow regions indicate the gain and the loss of electrons, respectively. Electrons transfer from Ta to N during the formation of the Ta-N bond. The electrons shared between the Ta and N atoms show the interaction of Ta and N, indicating the orbital hybridization of Ta-d and N-p. Moreover, in Figure 6a, the electron distribution is also found between two Ta atom layers in Ta_2N-I. That means there is an interaction between Ta and Ta atoms in Ta_2N-I. However, such a phenomenon becomes unapparent in Ta_2N-II, owing to the ordering change of N atoms, as shown in Figure 6b. It is clear that the electrons no longer accumulate around the Ta atoms like Ta_2N-I. It can be seen in Figure 6d,f that these electrons transfer and assemble around the new N atom layer formed in the Ta_2N-II. Thus, the ordering change of N atoms has an outstanding influence on the electron distribution of Ta_2N. As seen in Figure 6c–f, the electron distribution of Ta_2N-II is more homogeneous in the unit cell than that of Ta_2N-I, which may explain why the anisotropy of Ta_2N-I is stronger.

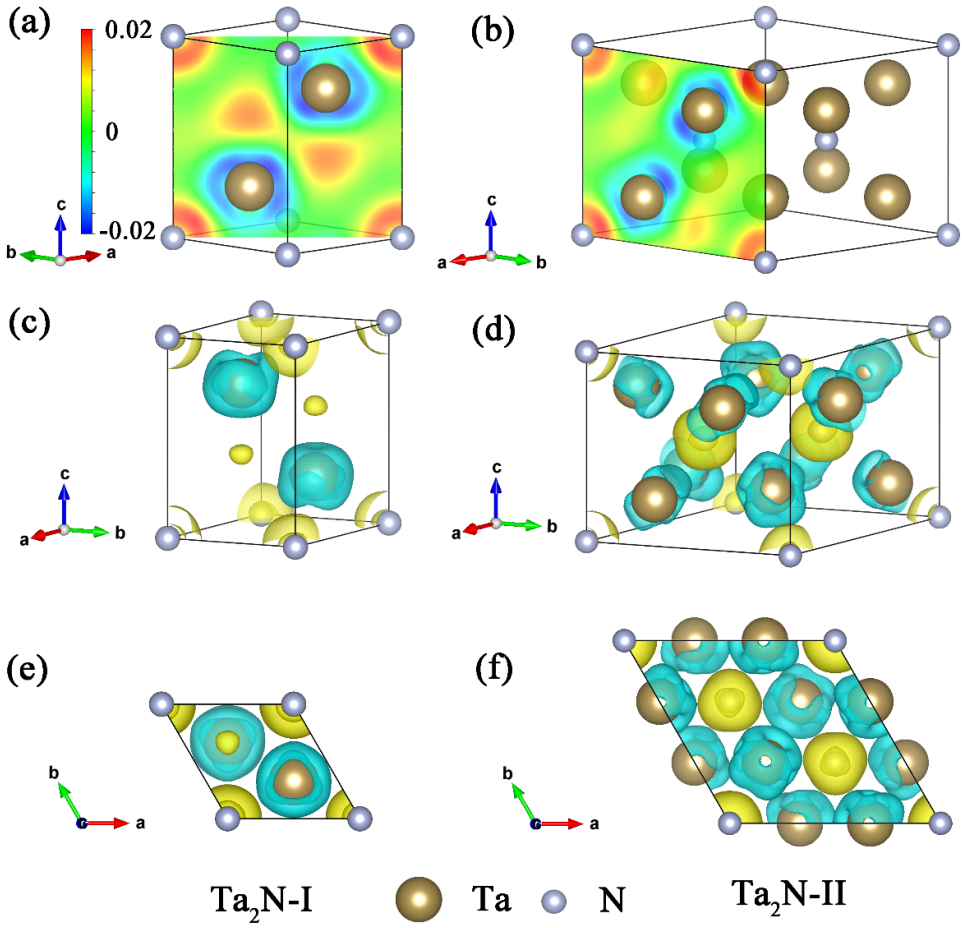

Figure 6. The sectional view of charge density difference of the (110) lattice plane in (**a**) Ta_2N-I and the (100) lattice plane in (**b**) Ta_2N-II. The side view and top view of charge density difference of (**c**,**e**) Ta_2N-I and (**d**,**f**) Ta_2N-II. The isosurface value is taken as 0.015 e/Å^3.

4. Conclusions

The stability, elastic, and electronic properties of Ta_2N-I and Ta_2N-II were investigated using DFT-based first-principles calculations. The calculated lattice parameters, enthalpies of formation, and elastic constants were a good match with the references, which confirms the reliability of our calculations. According to the enthalpy of formation, Ta_2N-II is energetically favorable compared to Ta_2N-I, due to the formation of a more stable atomic stacking model (N-Ta-N-Ta···) and the stronger covalent bond (Ta-N) in Ta_2N-II. As for the elastic properties, Ta_2N-II possesses a higher bulk modulus *B*, shear modulus *G*, and Youngs' modulus *E;* but a weaker anisotropy. Especially, a ductile-brittle transition was found between Ta_2N-I (ductile) and Ta_2N-II (brittle). It can be assumed from the partial density of states that both Ta_2N-I and Ta_2N-II are metallic. In addition, Ta_2N- II revealed the stronger orbital hybridization of Ta-d and N-p, resulting in stronger covalent bonding, which can explain the elevation of shear modulus. The charge density difference clearly illustrates the interaction of the Ta-N bond and electron distribution difference between Ta_2N-I and Ta_2N-II. These analyses of property differences, because of the ordering change of N atoms in Ta_2N compounds can further promote their application and research.

Author Contributions: Conceptualization, L.Z. and J.W.; data curation, L.Z.; formal analysis, L.Z., J.W. and S.-L.S.; funding acquisition, J.W.; investigation, L.Z.; methodology, L.Z. and J.W.; project administration, J.W. and Y.D., resources, J.W.; supervision, Y.D.; validation, J.W. and S.-L.S.; visualization, L.Z. and C.D.; writing—original draft, L.Z.; writing—review & editing, J.W., C.D., Y.D., S.-L.S. and Z.-K.L. All authors have read and agreed to the published version of the manuscript.

Funding: This research was funded by the National Key Research and Development Program of China (Materials Genome Initiative), grant number 2017YFB0701700, and the National Natural Science Foundation for Youth of China, grant number 51601228.

Data Availability Statement: The data presented in this study are available within the article.

Acknowledgments: First-principles calculations were partially carried out at the High Performance Computing of Central South University, which is greatly acknowledged.

Conflicts of Interest: The authors declare no conflict of interest.

References

1. Du, J.W.; Chen, L.; Chen, J.; Du, Y. Mechanical properties, thermal stability and oxidation resistance of TiN/CrN multilayer coatings. *Vacuum* **2020**, *179*, 109468. [CrossRef]
2. Navinšek, B.; Panjan, P.; Milošev, I. Industrial applications of CrN (PVD) coatings, deposited at high and low temperatures. *Surf. Coatings Technol.* **1997**, *97*, 182–191. [CrossRef]
3. Hu, C.; Xu, Y.X.; Chen, L.; Pei, F.; Du, Y. Mechanical properties, thermal stability and oxidation resistance of Ta-doped CrAlN coatings. *Surf. Coatings Technol.* **2019**, *368*, 25–32. [CrossRef]
4. Hu, C.; Guo, K.; Li, Y.; Gu, Z.; Quan, J.; Zhang, S.; Zheng, W. Optical coatings of durability based on transition metal nitrides. *Thin Solid Films* **2019**, *688*, 137339. [CrossRef]
5. Davis, R.F. III-V nitrides for electronic and optoelectronic applications. *Proc. IEEE* **1991**, *79*, 702–712. [CrossRef]
6. Ou, P.; Wang, J.; Shang, S.-L.; Chen, L.; Du, Y.; Liu, Z.-K.; Zheng, F. A first-principles study of structure, elasticity and thermal decomposition of $Ti_{1-x}TM_xN$ alloys (TM = Y, Zr, Nb, Hf, and Ta). *Surf. Coatings Technol.* **2015**, *264*, 41–48. [CrossRef]
7. Stampfl, C.; Freeman, A.J. Stable and metastable structures of the multiphase tantalum nitride system. *Phys. Rev. B* **2005**, *71*, 024111. [CrossRef]
8. Bernoulli, D.; Müller, U.; Schwarzenberger, M.; Hauert, R.; Spolenak, R. Magnetron sputter deposited tantalum and tantalum nitride thin films: An analysis of phase, hardness and composition. *Thin Solid Films* **2013**, *548*, 157–161. [CrossRef]
9. Garcia-Mendoza, T.; Martinez-Garcia, A.; Becerril-Juarez, I.; Lopez-Vazquez, E.; Avalos-Borja, M.; Valera-Zaragoza, M.; Juarez-Arellano, E. Mechanosynthesis of metastable cubic δ-$Ta_{1-x}N$. *Ceram. Int.* **2020**, *46*, 23049–23058. [CrossRef]
10. Hahn, R.; Koutná, N.; Wójcik, T.; Davydok, A.; Kolozsvári, S.; Krywka, C.; Holec, D.; Bartosik, M.; Mayrhofer, P.H. Mechanistic study of superlattice-enabled high toughness and hardness in MoN/TaN coatings. *Commun. Mater.* **2020**, *1*, 1–11. [CrossRef]
11. Xiao, Y.; Feng, C.; Fu, J.; Wang, F.; Li, C.; Kunzelmann, V.F.; Jiang, C.-M.; Nakabayashi, M.; Shibata, N.; Sharp, I.D.; et al. Band structure engineering and defect control of Ta_3N_5 for efficient photoelectrochemical water oxidation. *Nat. Catal.* **2020**, *3*, 932–940. [CrossRef]
12. Cancellieri, C.; Scott, E.A.; Braun, J.; King, S.W.; Oviedo, R.; Jezewski, C.; Richards, J.; La Mattina, F.; Jeurgens, L.P.H.; Hopkins, P.E. Interface and layer periodicity effects on the thermal conductivity of copper-based nanomultilayers with tungsten, tantalum, and tantalum nitride diffusion barriers. *J. Appl. Phys.* **2020**, *128*, 195302. [CrossRef]
13. Abadias, G.; Li, C.-H.; Belliard, L.; Hu, Q.M.; Greneche, N.; Djemia, P. Large influence of vacancies on the elastic constants of cubic epitaxial tantalum nitride layers grown by reactive magnetron sputtering. *Acta Mater.* **2020**, *184*, 254–266. [CrossRef]
14. Terao, N. Structure of Tantalum Nitrides. *Jpn. J. Appl. Phys.* **1971**, *10*, 248–259. [CrossRef]
15. Zerr, A.; Miehe, G.; Li, J.; Dzivenko, D.A.; Bulatov, V.K.; Hofer, H.; Bolfan-Casanova, N.; Fialin, M.; Brey, G.; Watanabe, T.; et al. High-Pressure Synthesis of Tantalum Nitride Having Orthorhombic U_2S_3 Structure. *Adv. Funct. Mater.* **2009**, *19*, 2282–2288. [CrossRef]
16. Strähle, J. Die Kristallstruktur des Tantal(V)-nitrids Ta_3N_5. *Z. Anorg. Allg. Chem.* **1973**, *402*, 47–57. [CrossRef]
17. Jiang, C.; Lin, Z.; Zhao, Y. Thermodynamic and Mechanical Stabilities of Tantalum Nitride. *Phys. Rev. Lett.* **2009**, *103*, 185501. [CrossRef] [PubMed]
18. Christensen, A.N.; Lebech, B. A reinvestigation of the structure of ε-tantalum nitride. *Acta Crystallogr. Sect. B Struct. Crystallogr. Cryst. Chem.* **1978**, *34*, 261–263. [CrossRef]
19. Conroy, L.; Christensen, A. Preparation and crystal structure of β-Ta_2N. *J. Solid State Chem.* **1977**, *20*, 205–207. [CrossRef]
20. Friedrich, A.; Winkler, B.; Bayarjargal, L.; Arellano, E.A.J.; Morgenroth, W.; Biehler, J.; Schröder, F.; Yan, J.; Clark, S.M. In situ observation of the reaction of tantalum with nitrogen in a laser heated diamond anvil cell. *J. Alloy. Compd.* **2010**, *502*, 5–12. [CrossRef]
21. Lee, T.-H.; Kim, S.-J.; Shin, E.; Takaki, S. On the crystal structure of Cr_2N precipitates in high-nitrogen austenitic stainless steel. III. Neutron diffraction study on the ordered Cr_2N superstructure. *Acta Crystallogr. Sect. B Struct. Sci.* **2006**, *62*, 979–986. [CrossRef] [PubMed]
22. Christensen, A.N.; Lebech, B. The structure of β-vanadium nitride. *Acta Crystallogr. Sect. B Struct. Crystallogr. Cryst. Chem.* **1979**, *35*, 2677–2678. [CrossRef]
23. Sahnoun, M.; Parlebas, J.; Driz, M.; Daul, C. Structural and electronic properties of isostructural transition metal nitrides. *Phys. B Condens. Matter.* **2010**, *405*, 3822–3825. [CrossRef]

24. Wang, J.; Ma, A.; Li, M.; Jiang, J.; Chen, J.; Jiang, Y. Chemical bonding and Cu diffusion at the Cu/Ta_2N interface: A DFT study. *Phys. Chem. Chem. Phys.* **2018**, *20*, 13566–13573. [CrossRef] [PubMed]
25. Yu, R.; Jiang, Y.; Zhou, R. First-principle studies of the stability, electronic and elastic properties of trigonal-type M_2N (M = Cr, V, Nb and Ta). *Solid State Commun.* **2014**, *186*, 32–37. [CrossRef]
26. Kresse, G.; Hafner, J. Ab initiomolecular dynamics for open-shell transition metals. *Phys. Rev. B* **1993**, *48*, 13115–13118. [CrossRef]
27. Kresse, G.; Hafner, J. Ab initiomolecular-dynamics simulation of the liquid-metal–amorphous-semiconductor transition in germanium. *Phys. Rev. B* **1994**, *49*, 14251–14269. [CrossRef] [PubMed]
28. Perdew, J.P.; Burke, K.; Ernzerhof, M. Generalized gradient approximation made simple. *Phys. Rev. Lett.* **1996**, *77*, 3865. [CrossRef]
29. Kresse, G.; Joubert, D. From ultrasoft pseudopotentials to the projector augmented-wave method. *Phys. Rev. B* **1999**, *59*, 1758–1775. [CrossRef]
30. Blöchl, P.E.; Jepsen, O.; Andersen, O.K. Improved tetrahedron method for Brillouin-zone integrations. *Phys. Rev. B* **1994**, *49*, 16223–16233. [CrossRef]
31. Birch, F. Finite Elastic Strain of Cubic Crystals. *Phys. Rev.* **1947**, *71*, 809–824. [CrossRef]
32. Birch, F. Finite strain isotherm and velocities for single-crystal and polycrystalline NaCl at high pressures and 300°K. *J. Geophys. Res. Space Phys.* **1978**, *83*, 1257–1268. [CrossRef]
33. Zhang, R.F.; Veprek, S.; Argon, A.S. Anisotropic ideal strengths and chemical bonding of wurtzite BN in comparison to zincblende BN. *Phys. Rev. B* **2008**, *77*, 172103. [CrossRef]
34. Shang, S.; Saengdeejing, A.; Mei, Z.; Kim, D.; Zhang, H.; Ganeshan, S.; Wang, Y.; Liu, Z. First-principles calculations of pure elements: Equations of state and elastic stiffness constants. *Comput. Mater. Sci.* **2010**, *48*, 813–826. [CrossRef]
35. Wang, J.; Shang, S.-L.; Wang, Y.; Mei, Z.-G.; Liang, Y.-F.; Du, Y.; Liu, Z.-K. First-principles calculations of binary Al compounds: Enthalpies of formation and elastic properties. *Calphad* **2011**, *35*, 562–573. [CrossRef]
36. Wang, J.; Du, Y.; Tao, X.; Ouyang, Y.; Zhang, L.; Chen, Q.; Engström, A. First-principles generated mechanical property database for multi-component Al alloys: Focusing on Al-rich corner. *J. Min. Met. Sect. B Met.* **2017**, *53*, 1–7. [CrossRef]
37. Born, M.; Huang, K.; Lax, M. Dynamical Theory of Crystal Lattices. *Am. J. Phys.* **1955**, *23*, 474. [CrossRef]
38. Pham, D.C. Asymptotic estimates on uncertainty of the elastic moduli of completely random trigonal polycrystals. *Int. J. Solids Struct.* **2003**, *40*, 4911–4924. [CrossRef]
39. Hill, R. The Elastic Behaviour of a Crystalline Aggregate. *Proc. Phys. Soc. Sect. A* **1952**, *65*, 349–354. [CrossRef]
40. Ranganathan, S.I.; Ostoja-Starzewski, M. Universal Elastic Anisotropy Index. *Phys. Rev. Lett.* **2008**, *101*, 055504. [CrossRef]
41. Rogers, D. An introduction to applied anisotropic elasticityby R. F. S. Hearmon. *Acta Crystallogr.* **1962**, *15*, 625–626. [CrossRef]
42. Brauer, G.; Zapp, K.H. Die Nitride des Tantals. *Zeitschrift für Anorganische und Allgemeine Chemie* **1954**, *277*, 129–139. [CrossRef]
43. Lei, W.; Liu, D.; Zhang, J.; Shen, L.; Li, X.; Cui, Q.; Zou, G. Direct synthesis and characterization of single-phase tantalum nitride (Ta_2N) nanocrystallites by dc arc discharge. *J. Alloy. Compd.* **2008**, *459*, 298–301. [CrossRef]
44. Pugh, S. XCII. Relations between the elastic moduli and the plastic properties of polycrystalline pure metals. *Lond. Edinb. Dublin Philos. Mag. J. Sci.* **1954**, *45*, 823–843. [CrossRef]
45. Pettifor, D.G. Theoretical predictions of structure and related properties of intermetallics. *Mater. Sci. Technol.* **1992**, *8*, 345–349. [CrossRef]
46. Jhi, S.-H.; Ihm, J.; Louie, S.G.; Cohen, M.L. Electronic mechanism of hardness enhancement in transition-metal carbonitrides. *Nat. Cell Biol.* **1999**, *399*, 132–134. [CrossRef]